





Nonlinear thermal simulation of laser metal deposition

Diego Montoya-Zapata ^{a,b}, Juan M. Rodríguez^c, Aitor Moreno ^a, Oscar Ruiz-Salguero ^b
and Jorge Posada ^a

5 ^aVicomtech Foundation, Basque Research and Technology Alliance (BRTA), Donostia-San Sebastian, Spain; ^bLaboratory of Cad-Cam-Cae, Universidad Eafit, Medellín, Colombia; ^cDepartment of Mechanical Engineering, Universidad Eafit, Medellín, Colombia

ABSTRACT

Simulation of Laser Metal Deposition (LMD) is central to the planning of Additive Manufacturing processes. This manuscript presents the computational implementation of a 2D-plus-thickness nonlinear thermal simulation of LMD, which considers: (i) temperature-dependent material properties, (ii) heat losses due to convection and radiation, (iii) geometrical update during material deposition, (iv) phase change and (v) the interaction between the laser and the substrate. The implementation computes the history of the temperature field at a cross-cut normal to the laser trajectory and the history of the bead accumulation. The material deposition model is based on the spatial distribution of the delivered powder. This manuscript presents the mathematical and numerical foundations to execute an efficient local re-meshing of the growing bead. The numerical estimation of the bead geometry is compared with experimental results found in the existing literature. The present model shows reasonable accuracy to predict the bead width (15% error) and bead height (22% error). This implementation is an in-house one, which allows for the inclusion of additional physical effects. Additional work is needed to account for the particle (thermo) dynamics over the substrate, responsible for a significant material and energy waste, which in turn leads to the actual temperature and molten depth being over-estimated in the executed simulations.

ARTICLE HISTORY

Received 29 June 2021
Accepted 29 September 2021

KEYWORDS

Laser metal deposition;
additive manufacturing;
nonlinear finite element
method

1. Introduction

25 Laser Metal Deposition (LMD) is an additive manufacturing process in which metal powder is delivered on top of a substrate while a laser melts the added material to produce a new layer. LMD has gained importance during the last several years because of its applications in the repair, coating and manufacturing of high-valued industrial parts (Leino, Pekkarinen, and Soukka 2016).

This manuscript presents the implementation of a nonlinear 2D-plus-thickness thermal model for the simulation of LMD. The simplification is justified under the assumption of process stability along the direction of movement of the tool head. The laser energy source is modelled as a flux boundary condition. The present implementation considers the following aspects: (1) the variation of the material properties with respect to the temperature, (2) convection and radiation heat losses and (3) the dynamic evolution of the domain due to material deposition.

45 This manuscript reports the implementation of the Finite Element Method (FEM) for 2D triangular elements. This manuscript discusses the corresponding FEM matrices of the considered phenomena (heat equation, temperature-dependent material properties, radiation, and convection). A model for

the representation of the material addition based on the spatial distribution of the delivered powder is formulated. Its theoretical foundations and its integration into the Finite Element Analysis (FEA) analysis pipeline are also presented in this manuscript. 55

The remainder of this article is organised as follows: Section 2 provides a review of the previous works. Section 3 presents the governing equations, numerical schemes and the methods to model material deposition. Section 4 presents and discusses the results of the implementation. Section 5 concludes the manuscript and suggests potential future work. 60

2. Literature review

2.1. Simulation of laser metal deposition

Within LMD, recent studies (Corbin et al. 2017; El Cheikh et al. 2012; Goodarzi, Pekkarinen, and Salminen 2015; Ocelik et al. 2014; Nenadl et al. 2014) have employed physical experimentation and statistical techniques (e.g. design of experiments and ANOVA) to devise empirical models that link the process parameters with the final bead geometry. These studies have focused on the influence of the laser power, tool-head speed and mass feed rate on the height, width and dilution ratio of the final bead. 75

In LMD, the substrate and bead thermal histories are relevant because they allow the prediction of the mechanical properties, the microstructure and residual stresses of the workpiece (Cheng, Shrestha, and Chou 2016; Costa et al. 2002; Heigel, Michaleris, and Palmer 2015; Michaleris 2014; Montoya-Zapata et al. 2021b; Ravi et al. 2013). Authors have relied on numerical simulation to represent complex phenomena involved in the modelling of LMD. Pure thermal models (Michaleris 2014; Cordovilla et al. 2019; Ya, Pathiraj, and Liu 2016) have allowed the prediction of the thermal history of the melt-pool during deposition. Ref. (Ya, Pathiraj, and Liu 2016) presents a 2D thermal model that considers convection, radiation and phase change. The model is fed with the powder efficiency to estimate the final bead geometry and thermal history during deposition. The research in (Michaleris 2014) confirms the importance of considering convection and radiation heat losses to obtain accurate temperature estimations. Thermal models have also been used to study the impact of the process parameters on the resulting workpiece. In this regard, Cordovilla et al. (2019) uses a 2D thermal model to study the influence of the material flow rate, nozzle speed and laser power on the melting depth in the substrate.

Thermo-fluid models (Arrizubieta et al. 2017; Manvatkar, De, and DebRoy 2015; Tian et al. 2019) have incorporated fluid flow effects into the thermal simulations to study the dynamics of the melt-pool. Apart from the temperature, thermo-fluid models predict the velocity field in the melt-pool. Models in Refs. (Arrizubieta et al. 2017; Manvatkar, De, and DebRoy 2015) include Marangoni and capillary effects, which produce more accurate temperature predictions than pure thermal models. Tian et al (2019) uses a 2D thermal-fluid model to study the effects of the material flow rate and the laser power on the shape of the melt-pool.

Thermo-mechanical approaches (Caiazzo and Alfieri 2019; Farahmand and Kovacevic 2014; Stender et al. 2018) have calculated residual stresses and distortions by estimating the temperature and displacements during deposition. Farahmand and Kovacevic 2014 and Stender et al. 2018 consider the same phenomena as pure thermal models: radiation, convection, temperature-dependent properties and phase change phenomena. However, they include the effects of thermal expansion to execute solid mechanics analysis via the estimation of the displacement field. Farahmand and Kovacevic (2014) studies the residual stress in several contiguous single-layer tracks. Stender et al. (2018) analyzes the residual stress and distortion of multi-layer cylindrical geometries.

Most of the approaches mentioned above have been executed on commercial software and the implementation has not been discussed. More comprehensive

literature reviews on the simulation of LMD can be found in (Pinkerton 2015; Tamanna, Crouch, and Naher 2019).

2.2. Assessment of temperature predictions and computational resources

The experimental measurement of the temperature in the LMD process is a very challenging task. The high-temperature conditions of LMD make unfeasible the temperature measurement within the melt-pool. Researchers have used non-contact devices (e.g. infrared cameras and pyrometers) to gather temperature data of the melt-pool surface. The accuracy of the measurements of non-contact devices is affected by several conditions, such as (i) the interference of the laser and the powder metal, (ii) non-constant (unknown) thermal emissivity of the melt-pool and (iii) the calibration of the sensing devices (Chua, Ahn, and Moon 2017; Tang et al. 2020). As an alternative, other authors have used metallography as an indirect method to infer the temperature history in the LMD process (Cordovilla et al. 2019; Arrizubieta et al. 2017; Tian et al. 2019; Caiazzo and Alfieri 2019). Metallography is a destructive technique, which requires the cross-sectioning of the workpiece.

The authors in Cordovilla et al. (2019); Ya, Pathiraj, and Liu (2016), Arrizubieta et al. (2017), Tian et al. (2019), Caiazzo and Alfieri (2019) and Stender et al. (2018) do not report the execution times of the numerical simulation. The lack of this data is related to the use of commercial software. Commercial software does not inform the execution time of each subprocess of the simulation (e.g. remeshing, powder metal and laser interaction, and thermal/fluid/mechanical FEM solution). Michaleris (2014) informs the execution time of the simulation. However, the scope of the simulation and the mathematical models are different in each work. It is, therefore, unfeasible to compare the execution time of the simulation or its sub-process with other related studies.

2.3. Representation of the bead geometry

One of the main tasks in the numerical simulation of LMD is the representation of the deposited material. In the literature, two approaches can be identified. The first one pre-defines the cross-section of the final bead geometry. Several functions are used: circular and elliptical (El Cheikh et al. 2012; Ocelik et al. 2014; Nenadl et al. 2014; Zhou, Dai, and Zheng 2011), sinusoidal (Ocelik et al. 2014; Nenadl et al. 2014; Caiazzo and Alfieri 2019) and parabolic (Ya, Pathiraj, and Liu 2016; Tian et al. 2019). This approach does not represent the intermediate states of the bead geometry during the deposition.

In the second approach, the bead geometry is induced by the spatial (3D) distribution of the delivered metal powder delivered on top of the substrate. The powder metal distribution is modelled as a function of the process parameters (powder spatial flow rate profile and nozzle velocity) and material properties (density). Authors have used two functions: Gaussian (El Cheikh et al. 2012; Arrizubieta et al. 2017; Montoya-Zapata et al. 2021a; Taberero et al. 2010, 2013) and circular (El Cheikh et al. 2012). These models give a complete description of the amount and distribution of material on top of the substrate, which can be used to describe the evolution of the bead geometry during the deposition.

2.4. Conclusions of the literature review

This literature survey has identified the following numerical approaches to calculate the thermal history during the deposition in LMD: pure thermal, thermo-fluid and thermo-mechanical models. These approaches exploit the capabilities of numerical simulation to include complex phenomena, such as melt-pool dynamics, phase change, variation of the material properties with respect to the temperature, and radiation/convection/conduction heat losses. Many of these publications report the use of commercial software. Therefore, the discussion of the numerical implementation of the mathematical models is missing.

This manuscript presents an in-house implementation of a 2D-plus-thickness nonlinear simulation of LMD. Since no commercial FEA software is used, (i) it is flexible and extensible, (ii) it is particularised to LMD and (iii) the mathematical models are thoroughly presented and discussed. This manuscript reports a thermal model which considers: (i) temperature-dependent material properties, (ii) convection and radiation heat losses, (iii) material deposition and (iv) phase change. The energy input to the system is modelled as a boundary condition of the type flux. This flux occurs at the upper border of the FEA mesh, which contains both substrate and bead elements. This manuscript thus discusses the interaction among physical, mathematical, and numerical considerations in LMD simulation.

This manuscript also reports the remeshing strategy used between time frames. The addition of material causes a (constrained Delaunay) remeshing, which is confined to the bead domain alone. This strategy saves resources both for geometry and temperature field re-computing at successive time steps.

The implemented method does not model (i) laser and metal powder flight interaction, (ii) powder evaporation (c) powder scattering away from bead due to the gas jet dynamics, (d) fluid dynamics within the molten material.

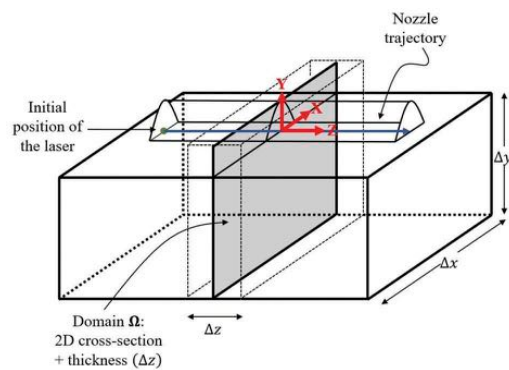


Figure 1. Simulation of the deposition of LMD. Graphical representation of the domain, reference frame and parameters involved.

3. Methodology

3.1. Problem description

This work aims to study the geometry and temperature evolution of a linear track of the Laser Metal Deposition process, as shown in Figure 1. This work considers that the process parameters (tool-head cruise speed, powder deposition rate and laser power) remain constant throughout the deposition. This study is limited to a 2D cross-section (plus thickness Δz). Features of the computer simulations follow.

1. Material deposition is considered. As a result, the bead cross cut and its FE mesh evolve as the time domain increases. This manuscript discusses the theoretical and numerical aspects of the material deposition model.

2. The energy delivered by the laser is modelled as a flux boundary condition that acts on the top of the domain.

3. The physical properties (density, specific heat and conductivity) of the substrate and the cladding materials are functions of the temperature. The simulation also contemplates the phase-change (from solid to liquid and vice-versa) of the substrate and cladding materials.

4. Heat loss due to radiation and convection is included.

5. The Newton-Raphson method is used to execute the nonlinear computation of temperature-dependent material properties, radiation/convection/conduction heat migration, and phase change.

6. This work does not consider molten metal fluid dynamics nor energy attenuation due to the interaction between the laser beam and the powder.

3.2. Governing equations

The present work uses the heat equation to describe the temperature distribution $T(\mathbf{x}, t)$ in the 2D domain Ω

$$\rho C \frac{\partial T}{\partial t} - \nabla \cdot (\kappa \nabla T) = s \quad (1)$$

where ρ , C and κ denote the density, specific heat and thermal conductivity, respectively. This work considers that the material properties depend on the temperature. The function $s = s(\mathbf{x}, t)$ represents the heat source (which in this case is equal to 0).

At the beginning of the simulation, the domain is at room temperature (300 K):

$$T(\mathbf{x}, 0) = T^0(\mathbf{x}) = 300 \quad (2)$$

Temperature (Dirichlet) and flux (Neumann) conditions may be imposed on the boundary of Ω ($\partial\Omega$). The regions of $\partial\Omega$ with imposed Dirichlet and Neumann boundary conditions are denoted as $\partial\Omega_T$ and $\partial\Omega_q$, respectively. They fulfill the following conditions:

$$\partial\Omega_T \cup \partial\Omega_q = \partial\Omega; \quad \partial\Omega_T \cap \partial\Omega_q = \emptyset \quad (3)$$

The boundary conditions are formally stated as follows:

$$\begin{aligned} T(\mathbf{x}, t) &= \bar{T}(\mathbf{x}, t), & \mathbf{x} \in \partial\Omega_T; \\ \mathbf{q}(\mathbf{x}, t) \cdot \mathbf{n}(\mathbf{x}) &= \bar{q}(\mathbf{x}, t), & \mathbf{x} \in \partial\Omega_q \end{aligned} \quad (4)$$

where \bar{T} and \bar{q} are known scalar functions, and \mathbf{n} is the normal vector that points outwards. The heat flux \mathbf{q} satisfies the Fourier law $\mathbf{q} = -\kappa \nabla T$.

3.2.1. Weak form and finite element discretisation

The weak form of the problem stated in Equations (1)–(4) is given by:

$$\begin{aligned} \int_{\Omega} w \rho C \frac{\partial T}{\partial t} dV + \int_{\Omega} \nabla w \cdot (\kappa \nabla T) dV \\ = \int_{\Omega} w s dV - \int_{\partial\Omega_q} w \bar{q} dA \end{aligned} \quad (5)$$

where w is a weighting function. The differential elements of volume and area in Equation (5) become $dV = \Delta z dA$ and $dA = \Delta z dL$ where Δz is the thickness of Ω .

To find an approximate solution of the temperature field T , the domain Ω is partitioned into (3-node) triangular finite elements Ω^e . Say T^h is the approximated solution for T . The interpolation of T^h in the triangular element Ω^e is given by

$$T^h(\mathbf{x}, t) = \sum_{a=1}^3 N_a(\mathbf{x})^e \theta_a(t), \quad \mathbf{x} \in \Omega^e \quad (6)$$

where $\theta_a(t)$ is the temperature at node a of the element Ω^e . The functions N_1, N_2 and N_3 are the shape functions for the triangular FEA elements. They also define the mapping between a reference triangle Ω^ξ with vertices $\{(0, 0), (1, 0), (0, 1)\}$ and any element Ω^e in the FEA mesh (see Figure 2(a)):

$$\begin{aligned} N_1(\xi, \eta) &= 1 - \xi - \eta; & N_2(\xi, \eta) &= \xi; & N_3(\xi, \eta) &= \eta; \\ \xi, \eta &\in [0, 1] \end{aligned} \quad (7)$$

After the spatial discretisation, the semi-discrete (discrete in space and continuous in time) formulation for Equation (5) is obtained:

$$\mathbb{M} \dot{\theta} + \mathbb{K} \theta - \mathbf{f} = 0 \quad (8)$$

where the vector of nodal temperatures $\theta(t)$ is a continuous function of time. The components of the mass and conductivity matrices, $\mathbb{M}(t)$ and $\mathbb{K}(t)$, are

$${}^e \mathbb{M}_{ab} = \int_{\Omega^e} \rho C N_a N_b \Delta z dA; \quad a, b = 1, 2, 3 \quad (9)$$

$${}^e \mathbb{K}_{ab} = \int_{\Omega^e} \nabla N_a \cdot (\kappa \nabla N_b) \Delta z dA; \quad a, b = 1, 2, 3 \quad (10)$$

Let $\partial\Omega_q^e$ be the edge of the element Ω^e that is subjected to flux boundary conditions. The interpolation for the temperature along the edge $T^h(\mathbf{x}, t)$ is given by

$$T^h(\mathbf{x}, t) = \sum_{a=1}^2 N_a^q(\mathbf{x})^e \theta_a(t); \quad \mathbf{x} \in \partial\Omega^e \quad (11)$$

The functions N_1^q and N_2^q are the shape functions for the mapping between a reference segment $\partial\Omega^\xi$ with vertices $\{(0, 0), (1, 0)\}$ and any triangle segment $\partial\Omega_q^e$ in the FEA mesh (see Figure 2(b)):

$$N_1^q(\xi) = 1 - \xi; \quad N_2^q(\xi) = \xi \quad (12)$$

The components of the local force vector ${}^e \mathbf{f}(t)$ are

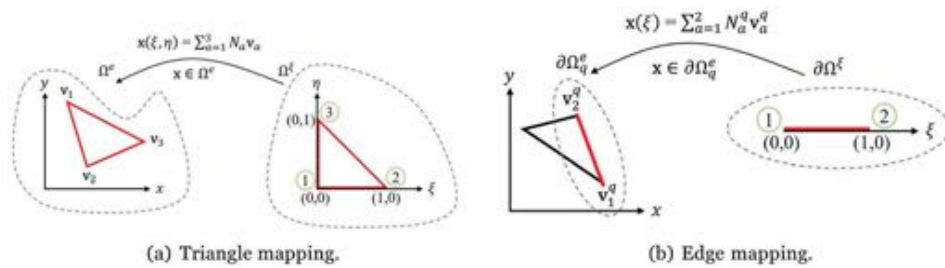


Figure 2. Mapping between the reference entities (triangle/edge) and the ones in the FEA mesh.

$${}^e f_a = \int_{\Omega^e} N_a s \Delta z dA - \int_{\partial\Omega_q^e} N_a^q \bar{q} \Delta z dL; \quad a = 1, 2 \quad (13)$$

The simulations in the present work **does** not consider heat sources ($s = 0$). The function $\bar{q} : \bar{q}(\mathbf{x}, t)$ accounts for the flux boundary conditions that are consider: the energy input of the laser \bar{q}_l , radiation \bar{q}_{rad} and convection \bar{q}_{conv} . The corresponding functions associated to each flux boundary condition are described in detail in the following sections.

Temperature (Dirichlet) boundary conditions are applied at the bottom of the domain. The temperature in this region is set to $\bar{T} = 300$ K during all the simulation.

3.2.2. Time discretisation and Newton-Raphson scheme

To obtain the fully discrete formulation of Equation (8) it is still necessary to execute the time discretisation. The simulation time interval $[0, t_{max}]$ is divided into N sub-intervals: $[t^0, t^1], [t^1, t^2], \dots, [t^{N-1}, t^N]$, such that $t^0 = 0$ and $t^N = t_{max}$.

The vector $\theta^s = \theta(t^s)$ denotes the nodal temperatures at t^s . The backward Euler method is used for the time discretisation by approximating the time derivative $\dot{\theta}^s$ as follows (Ibrahimbegovic 2009):

$$\dot{\theta}^s \approx \frac{\theta^s - \theta^{s-1}}{\Delta t} \quad (14)$$

Equation (14) is inserted into Equation (8). The reader may notice that, since ρ, C, κ and \bar{q} depend on the temperature, $\mathbb{M}^s, \mathbb{K}^s$ and \mathbf{f}^s are functions of the temperature (see Equations (9), (10) and (13)). Therefore, at every instant t^s , one obtains a system of nonlinear equations \mathbf{R} in which the variables are the nodal temperatures θ^s

$$\mathbf{R}(\theta^s) = \mathbb{M}^s(\theta^s - \theta^{s-1}) + \Delta t \mathbb{K}^s \theta^s - \Delta t \mathbf{f}^s = 0 \quad (15)$$

The Newton-Raphson scheme is used to solve this system of equations. The characteristics of this method requires several iterations to solve for θ^s at every time instant t^s . Let $\theta^{s,k}$ be the nodal temperature at iteration k . The Newton-Raphson updating rule for iteration k is given by

$$\theta^{s,k} = \theta^{s,k-1} + u; \quad u = -\left. \frac{d\mathbf{R}}{d\theta^s} \right|_{\theta^{s,k}} \mathbf{R}(\theta^{s,k}) \quad (16)$$

The matrix $\frac{d\mathbf{R}}{d\theta^s}$ is known as the tangent matrix. It is equal to:

$$\frac{d\mathbf{R}}{d\theta^s} = \frac{d\mathbf{h}^s}{d\theta^s} - \Delta t \frac{d\mathbf{f}^s}{d\theta^s} \quad (17)$$

where \mathbf{h}^s is the following vector

$$\mathbf{h}^s = \mathbb{M}^s(\theta^s - \theta^{s-1}) + \Delta t \mathbb{K}^s \theta^s \quad (18)$$

In the following sections, the components of the matrix $\frac{d\mathbf{R}}{d\theta^s}$ are discussed.

365

3.3. Model of the energy provided by the laser

The energy of the laser is modelled as a flux (or Neumann) boundary condition that acts on the top boundary of the domain Ω . This work uses the approach in Ref. (Caiazzo and Alfieri 2019) to calculate the corresponding heat flux. The function $I(x, z)$ [W/mm²] describes the energy distribution of the laser on the plane XZ, parallel to the substrate surface.

Let Ω^e be an FE element whose edge $\partial\Omega^e$ is at the top boundary. Let $\partial\Omega_{proj}^e$ be the projection of $\partial\Omega^e$ onto the plane XZ. Let R^e be the extrusion in direction Z, with thickness Δz , of $\partial\Omega_{proj}^e$ (see Figure 3). The input power P^e [W] and the corresponding heat flux \bar{q}_l^e [W/mm²] at $\partial\Omega^e$ are

$$P^e = \int_{R^e} I(x, z) dA; \quad \bar{q}_l^e = \frac{1}{\Delta z} \frac{P^e}{|\partial\Omega_{proj}^e|}. \quad (19)$$

Since the laser moves in Z direction, the laser intensity function I is also a function of time. Therefore, the heat flux over each edge must be calculated at every time step of the simulation.

The present work uses a Gaussian laser energy distribution:

$$I(x, z, t) = \frac{2\lambda P_L}{\pi R_L^2} \exp\left(-\frac{2((x - P_x(t))^2 + (z - P_z(t))^2)}{R_L^2}\right) \quad (20)$$

385

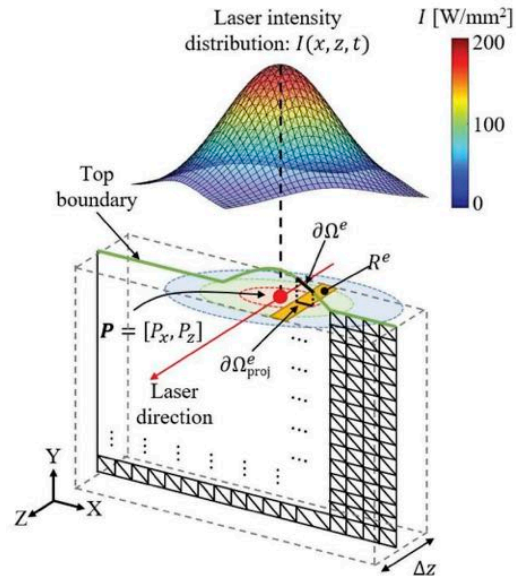


Figure 3. Calculation of the laser heat flux. Only the laser power that lies inside Ω (dotted lines) is considered.

where P_L is the laser power, λ is the laser absorption efficiency, R_L is the laser beam radius and $P = (P_x, P_y)$ is the laser position. Figure 3 shows a graphical representation of the process to compute the input heat flux associated to the energy provided by the laser.

3.4. Temperature-dependent material properties

This work considers that the material thermal properties ρ , C and κ depend on the temperature. This section provides the framework to include this consideration into the numerical scheme.

Recalling Equation (18), the component of the local vector ${}^e\mathbf{h}^s$ at node a is:

$${}^e\mathbf{h}_a^s = \sum_{b=1}^3 {}^e\mathbb{M}_{ab}^s ({}^e\theta_b^s - {}^e\theta_b^{s-1}) + \Delta t \sum_{b=1}^3 {}^e\mathbb{K}_{ab}^s {}^e\theta_b^s; \quad (21)$$

$a = 1, 2, 3$

The corresponding contribution to the tangent matrix $\frac{d\mathbf{R}}{d\theta^e}$ (Equation (17)) is given by:

$$\begin{aligned} \frac{\partial {}^e\mathbf{h}_a^s}{\partial {}^e\theta_c^s} = & {}^e\mathbb{M}_{ac}^s + \sum_{b=1}^3 \frac{\partial {}^e\mathbb{M}_{ac}^s}{\partial {}^e\theta_c^s} ({}^e\theta_b^s - {}^e\theta_b^{s-1}) \\ & + \Delta t \left({}^e\mathbb{K}_{ac}^s + \sum_{b=1}^3 \frac{\partial {}^e\mathbb{K}_{ac}^s}{\partial {}^e\theta_c^s} {}^e\theta_b^s \right); \quad (22) \end{aligned}$$

$a, c = 1, 2, 3$

Recalling Equations (9) and (10):

$$\begin{aligned} \frac{\partial {}^e\mathbf{h}_a^s}{\partial {}^e\theta_c^s} = & {}^e\mathbb{M}_{ac}^s \\ & + \sum_{b=1}^3 \left(\int_{\Omega^e} \frac{\partial(\rho C)}{\partial {}^e\theta_c^s} N_a N_b \Delta z dA \right) ({}^e\theta_b^s - {}^e\theta_b^{s-1}) + \\ & \Delta t \left({}^e\mathbb{K}_{ac}^s + \sum_{b=1}^3 \left(\int_{\Omega^e} \sum_{i=1}^2 \frac{\partial N_a}{\partial x_i} \frac{\partial \kappa}{\partial {}^e\theta_c^s} \frac{\partial N_b}{\partial x_i} \Delta z dA \right) {}^e\theta_b^s \right) \end{aligned} \quad (23)$$

$$\begin{aligned} = & {}^e\mathbb{M}_{ac}^s \\ & + \sum_{b=1}^3 \left(\int_{\Omega^e} \left(\rho \frac{\partial C}{\partial T} + C \frac{\partial \rho}{\partial T} \right) N_a N_b N_c \Delta z dA \right) ({}^e\theta_b^s - {}^e\theta_b^{s-1}) \\ & + \\ & \Delta t \left({}^e\mathbb{K}_{ac}^s + \sum_{b=1}^3 \left(\int_{\Omega^e} \sum_{i=1}^2 \frac{\partial N_a}{\partial x_i} \frac{\partial \kappa}{\partial T} N_c \frac{\partial N_b}{\partial x_i} \Delta z dA \right) {}^e\theta_b^s \right) \end{aligned} \quad (24)$$

The present work uses numerical integration (Gauss quadrature) to evaluate the integrals described above.

3.5. Phase change

The present work uses the equivalent specific heat method (Bergheau and Fortunier 2008) to model the change of state (from solid to liquid and vice-versa). In this approach, the phase change is modelled by modifying the specific heat of the material C . The new function is called the equivalent specific heat C_{eq} and it must add the energy of the latent heat of fusion L [J/kg] into the specific heat of the material in the temperature range $T \in [T_s, T_l]$ where the phase change occurs.

This work uses the following equivalent specific heat C_{eq} (Mayi et al. 2020) function:

$$C_{eq}(T) = C(T) + \frac{2L}{\sqrt{\pi}\Delta T} \exp\left(-\left(\frac{T - T_m}{\Delta T/2}\right)^2\right) \quad (25)$$

where $T_m = (T_s + T_l)/2$ and $\Delta T = T_l - T_s$

3.6. Convection and radiation heat losses

This work considers heat losses due to convection and radiation during the cladding process. Both radiation and convection are included into the model as flux (Neumann) boundary conditions. The regions of the domain subjected to heat loss considerations are the top, left- and right-hand sides of the domain.

Given the convection coefficient h_c and the ambient temperature T_∞ , the convection heat loss is accounted as $\bar{q}_{conv} = h_c(T - T_\infty)$. Using the interpolation of the temperature (Equation (11)) along the edge with flux boundary condition:

$$\bar{q}_{conv} = h_c \left(\sum_{b=1}^2 N_b^q(\mathbf{x}) {}^e\theta_b(t) - T_\infty \right), \quad (26)$$

Given the thermal emissivity ε and the Stefan-Boltzmann constant $\sigma \approx 5.67 \times 10^{-8}$ [W/(m² K⁴)], the radiation heat loss is represented by $\bar{q}_{rad} = \varepsilon\sigma(T^4 - T_\infty^4)$. Applying Equation (11) for the temperature interpolation:

$$\bar{q}_{rad} = \varepsilon\sigma \left(\left(\sum_{b=1}^2 N_b^q(\mathbf{x}) {}^e\theta_b(t) \right)^4 - T_\infty^4 \right), \quad (27)$$

To ease the readability of the Equations (28)–(31), one may drop the indices e and s of the components of the vector of nodal temperatures ${}^e\theta^s = [\theta_1, \theta_2]^T$ of the edge $\partial\Omega_q^e$ subjected to radiation and convection.

Equation (13) is applied to calculate the local force vector associated to the convection and radiation boundary conditions:

$${}^e\mathbf{f}_{conv}^s = \frac{\Delta z |\partial\Omega_q^e| h_c}{6} \begin{bmatrix} 2 & 1 \\ 1 & 2 \end{bmatrix} \begin{bmatrix} \theta_1 \\ \theta_2 \end{bmatrix} - \frac{\Delta z |\partial\Omega_q^e| h_c}{2} \begin{bmatrix} T_\infty \\ T_\infty \end{bmatrix} \quad (28)$$

$$e_{\text{rad}}^{\text{fs}} = \frac{\Delta z |\partial \Omega_q^e| \varepsilon \sigma}{30} \begin{bmatrix} 5 & 4 & 3 & 2 & 1 \\ 1 & 2 & 3 & 4 & 5 \end{bmatrix} \begin{bmatrix} \theta_1^4 \\ \theta_1^3 \theta_2 \\ \theta_1^2 \theta_2^2 \\ \theta_1 \theta_2^3 \\ \theta_2^4 \end{bmatrix} - \frac{\Delta z |\partial \Omega_q^e| h_c}{2} \begin{bmatrix} T_\infty^4 \\ T_\infty^4 \end{bmatrix} \quad (29)$$

The contributions of the radiation and convection to the local tangent matrix are:

$$\frac{d^e \mathbf{f}_{\text{conv}}^s}{d^e \theta^s} = \frac{\Delta z |\partial \Omega_q^e| h_c}{6} \begin{bmatrix} 2 & 1 \\ 1 & 2 \end{bmatrix} \quad (30)$$

$$\frac{d^e \mathbf{f}_{\text{rad}}^s}{d^e \theta^s} = \frac{\Delta z |\partial \Omega_q^e| \varepsilon \sigma}{30} \begin{bmatrix} 5 & 4 & 3 & 2 & 1 \\ 1 & 2 & 3 & 4 & 5 \end{bmatrix} \begin{bmatrix} 4\theta_1^3 & 0 \\ 3\theta_1^2 \theta_2 & \theta_1^3 \\ 2\theta_1 \theta_2^2 & 2\theta_1^2 \theta_2 \\ \theta_2^3 & 3\theta_1 \theta_2^2 \\ 0 & 4\theta_2^3 \end{bmatrix} \quad (31)$$

where $|\partial \Omega_q^e|$ is the length of the edge.

3.7. Material deposition

During the deposition stage, the shape of the bead is induced by the distribution of powder particles delivered by the nozzle. The function $f(x, z, t)$ [kg/(mm² s)] represents the powder particle density projected by the nozzle on top of the substrate. The present model assumes f follows a Gaussian distribution:

$$f(x, z, t) = \frac{2\mu}{\pi R_L^2} \exp\left(\frac{-2((x - P_x(t))^2 + (z - P_z(t))^2)}{R_L^2}\right) \quad (32)$$

where μ is the material flow rate [kg/s] and $P(t) = (P_x(t), P_z(t))$ is the laser position at time t .

The height H [mm] at time t is given by:

$$H(x, z, t) = \frac{1}{\rho_p} \int_0^t f(x, z, \xi) d\xi \quad (33)$$

where ρ_p is the density of the cladding material

Given Equation (33), the height grow rate is obtained:

$$\frac{\partial H(x, z, t)}{\partial t} = \frac{1}{\rho_p} f(x, z, t) \quad (34)$$

Equation (34) approximates the height change ΔH for the given time increment Δt . Material is added if the temperature on the top boundary is higher than the melting point of the deposited material.

3.8. Remeshing strategy

In the implementation reported, there are two meshes: substrate mesh and bead mesh. The substrate mesh remains constant with respect to the time evolution. However, the substrate mesh varies with respect to the space. The mesh is finer in the neighbourhoods of the laser impact point (Figure 4).

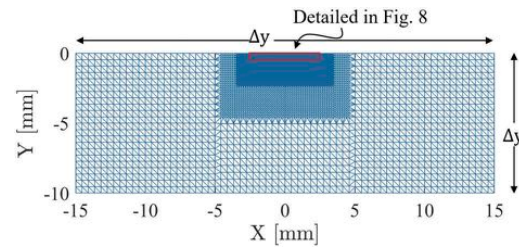


Figure 4. FEA mesh of the substrate.

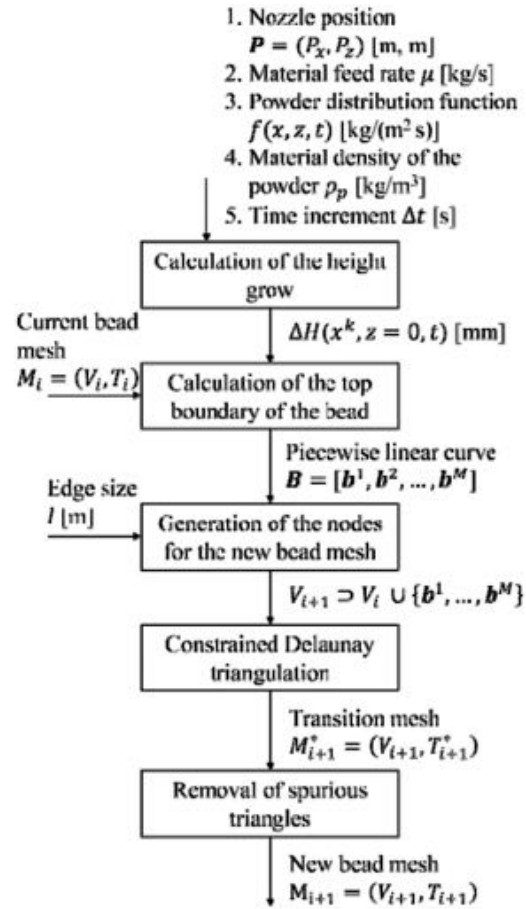


Figure 5. Remeshing strategy. Workflow for the generation of the bead mesh at every time step.

The bead mesh, on the other hand, must be updated at every time step. Figure 5 shows the proposed procedure to conduct the bead remeshing. A description of this procedure follows

1. **Calculation of the bead grow:** Let $X^{\text{top}} = \{x^1, x^2, \dots, x^T\}$, $x^k \in \mathbb{R}$, be the x-coordinates of the FEA nodes on top of the substrate (see Figure 6(a)). Equation (34) is used to calculate the height grow ΔH at $z = 0$ for every x^k ($k = 1, \dots, T$). The information required to execute this step is: (i) the nozzle position $P = (P_x, P_z)$, (ii) the material feed rate μ [kg/s], (iii) the powder particle distribution function $f(x, z, t)$ [kg/(m² s)], (iv) the density of the powder material ρ_p [kg/m³] and (v) the time increment Δt [s].

2. **Calculation of the top boundary of the bead:** Let $M_i = (V_i, T_i)$, with V_i as the set of nodes and T_i as the set of triangles, be the bead mesh at time step i . Given the mesh M_i and the height grow ΔH , the piecewise linear (PL) curve $B = [b^1, b^2, \dots, b^M]$, $b^k \in \mathbb{R}^2$, that describes the top boundary of the new mesh is calculated. The x-coordinate of every vertex $b^k = (b_x^k, b_y^k) \in B$ belongs to X^{top} ($b_x^k \in X^{\text{top}}$). Figure 6(b) shows an example of the resulting PL curve B .

3. **Generation of the FEA nodes:** Let V_{i+1} denote the set of nodes of the bead mesh at time step $i + 1$. Firstly, V_{i+1} contains the nodes of the previous mesh V_i and the vertices of B

$$V_{i+1} \supset V_i \cup \{b^1, \dots, b^M\}. \quad (35)$$

Given the goal edge length l [m], new nodes are added to V_{i+1} when: (i) the height grow is large ($\Delta H(x^k, z = 0) > l$) and (ii) the segments of B are long ($\|b^{k+1} - b^k\| > l$), as shown in Figure 6(b).

4. **Mesh generation:** A mesh $M_{i+1}^* = (V_{i+1}, T_{i+1}^*)$ is generated using constrained Delaunay triangulation (Carbonell, Rodriguez, and Oñate 2020; Rodriguez et al. 2016). The constraints of the triangulation are given by the edges of the bead boundary B . The triangulation may contain spurious triangles that do not belong to the bead (see Figure 6(c)). These spurious triangles are removed to produce the bead mesh for time step $i + 1$: $M_{i+1} = (V_{i+1}, T_{i+1})$, $T_{i+1} \subset T_{i+1}^*$, as shown in Figure 6(d).

In this work, triangular elements are preferred over other topologies (e.g. quadrilateral) because they straightforwardly adapt to the geometry of the growing bead. The quadrangular elements present singularities when 2 nodes coincide, which is unavoidable in corners whose geometry – topology is triangular.

3.8.1. Evaluation of the remeshing strategy

The time complexity of the proposed remeshing method is dictated by the time complexity of the Delaunay triangulation. The time complexity of the Delaunay triangulation is $\mathcal{O}(N \log N)$ (Shewchuk

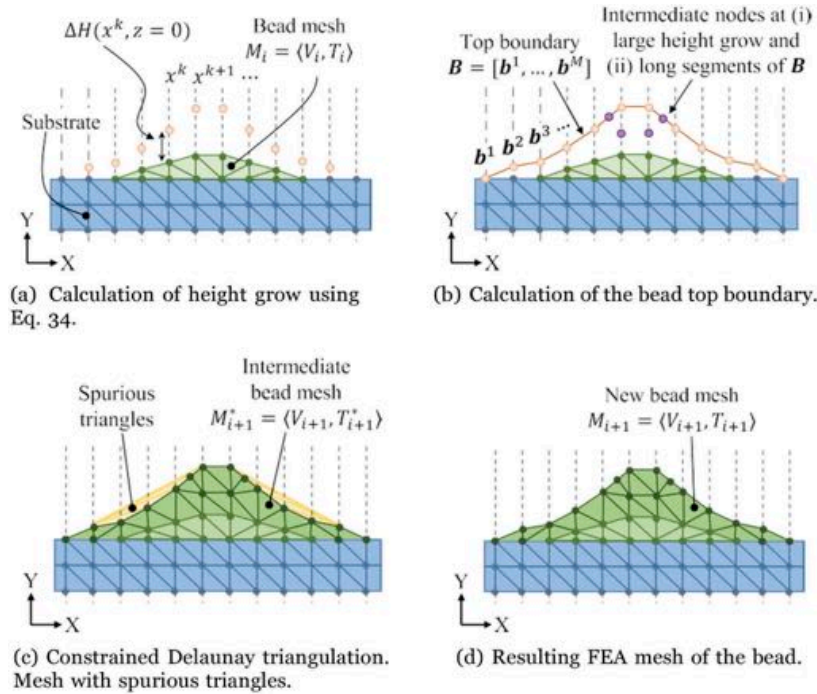


Figure 6. Graphical description of the stages of the remeshing strategy.

Table 1. Meshing and remeshing methods. Time complexity.

Method	Time complexity	Advantages	Limitations
Proposed method	$\mathcal{O}(N \log N)$ (Shewchuk 1996, Engwirda 2014)	(i) Good mesh quality and (ii) avoids temperature re-computing	High computational cost
Advancing-front method	$\mathcal{O}(N \log N)$ (Engwirda 2014)	Very good mesh quality	Requires temperature re-computing
Delaunay-based method	$\mathcal{O}(N \log N)$ (Engwirda 2014)	Very good mesh quality	Requires temperature re-computing
Laplacian smoothing method	$\mathcal{O}(N)$ (Sorkine et al. 2004)	Computational efficient	(i) Mesh quality is compromised and (ii) requires temperature re-computing
Spring-based smoothing method	$\mathcal{O}(N)$ (Bakhshi 2018)	Computational efficient	(i) Mesh quality is compromised and (ii) requires temperature re-computing

1996; Engwirda 2014), where N is the number of nodes in the triangulation. In this case, N corresponds to the number of nodes in the bead mesh. Table 1 presents the time complexity of other relevant methods used for 2D FEA remeshing: (i) advancing-front methods, (ii) Delaunay-based methods, (iii) Laplacian smoothing and (iv) spring-based smoothing. Methods (i)-(ii) are pure meshing procedures while methods (iii)-(iv) are smoothing procedures used in the context of remeshing.

The proposed remeshing method has the same time complexity ($\mathcal{O}(N \log N)$) as the other two pure meshing methods. Smoothing methods, on the other hand, have lower time complexity ($\mathcal{O}(N)$) but produce lower quality meshes (Engwirda 2014).

The proposed approach avoids nodes removal or node repositioning. It is advantageous compared to other remeshing approaches because (i) it is confined to the bead domain alone and (ii) the temperature field must not be re-computed when the bead mesh is updated. Since nodes are not repositioned, the representation of the deposited material requires additional nodes. Therefore, the number of nodes in the bead mesh increases at every time step, which leads to higher simulation time at every time step.

3.9. Material properties for the computational simulations

Cordovilla et al. (2019) executed several LMD experiments with an IPG Photonics YLS-6000 fibre laser of wavelength 900 nm. Cordovilla et al. (2019) used S355

Table 2. Material properties of the substrate material (S355) (Zhu, Khurshid, and Barsoum 2019) and cladding material (AISI 316L) (Mills 2002) used in the numerical simulations.

Property	S355	AISI 316L
Density ρ	7840 kg/m ³	7950 kg/m ³
Thermal conductivity κ	See Figure 7(a)	See Figure 7(a)
Specific heat C_p	See Figure 7(b)	See Figure 7(b)
Latent heat of fusion L	2.7×10^4 J/K	2.7×10^4 J/K
Solidus temperature T_s	1673 K	1658 K
Liquidus temperature T_l	1778 K	1723 K
Melting point T_m	1725.5 K	1690.5 K

carbon steel as substrate and AISI 316L stainless steel as cladding material. These same materials were used for the numerical simulations. The physical properties of S355 and AISI 316L are listed in Table 2. The thermal conductivity κ and specific heat C are considered as functions of the temperature (Zhu, Khurshid, and Barsoum 2019; Mills 2002), as shown in Figure 7(a,b). The equivalent specific heat is calculated using Equation (25). The resulting functions are shown in Figure 7(c). In order to compare the numerical results with the experimental results in Cordovilla et al. (2019), the simulations use the same domain size and process parameters reported in (Cordovilla et al. 2019).

4. Results

Regarding LMD simulation, the present implementation computes the time history of bead geometry and temperature field as well as the substrate temperature field. These computations are carried out in a substrate cross cut $\Delta x \times \Delta y$ (with thickness Δz) which is normal to the laser velocity (v_z). The powder feed μ , laser

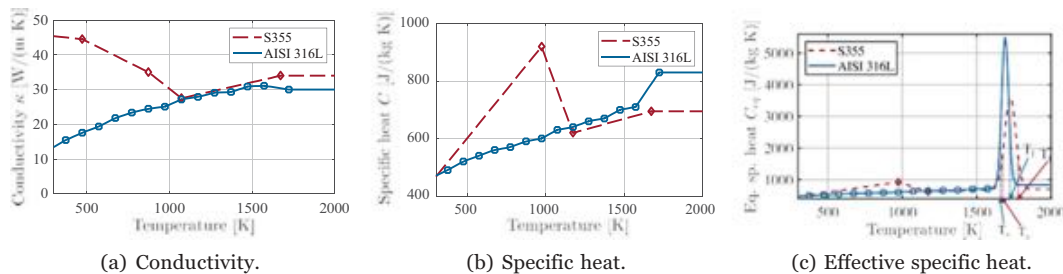

Figure 7. Material properties of the substrate material (S355) and cladding material (AISI 316L). Figures built using the data in References (Zhu, Khurshid, and Barsoum 2019; Mills 2002).

Table 3. Domain size and process parameters used for the numerical simulations.

Parameter	Value
Width (size in X) of the substrate Δx	30 mm
Height (size in Y) of the substrate Δy	10 mm
Thickness of the domain Δz	4.6 mm
Laser power 2800 W	
Laser absorption efficiency λ	0.6
Laser radius R_L	2.3 mm
Laser speed v_z	10 mm/s
Powder flow rate μ	0.3×10^{-3} kg/s
Initial position of the laser	[0, 0, -4.6]
Ambient temperature T_∞	300 K
Convection coefficient h_c	20 W/(m ² K)
Emissivity ϵ	0.5
Total simulation time	2.44 s
Number of time steps	90
Time increment (Δt)	0.027 s

570 power P_L and laser cruise speed v_z are constant during
the simulation. The parameters used in the numerical
simulation are listed in Table 3. The time increment Δt
between time steps was constant during the simula-
tion. This parameter was empirically set to guarantee
575 the convergence of the Newton-Raphson method, and
to avoid abrupt changes in the geometry and tempera-
ture of the domain.

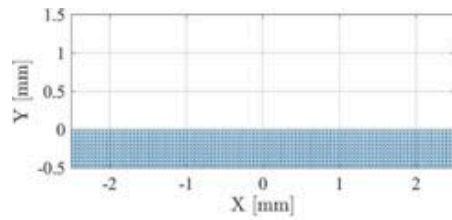
Figure 4 displays the FEA mesh of the substrate
domain, which remained constant along the time-
axis simulation. The mesh presents increased levels
580

of detail in the neighbourhoods receiving the metal
powder and the laser impact. Preliminary simulations
without considering material addition were conducted
to determine the size of the FEA elements. The sub-
strate mesh used for LMD simulation shown in
585 Figure 4 has 17213 triangular elements. The average
edge length in the most detailed zone is 0.05 mm,
which is in concordance with the values reported in
the literature (Ya, Pathiraj, and Liu 2016; Tian et al.
590 2019). The aspect ratio is lower than 2 for 98% of
the triangles, and lower than 3 for 100% of the tri-
angles. Thus, this substrate mesh presents very good quality.

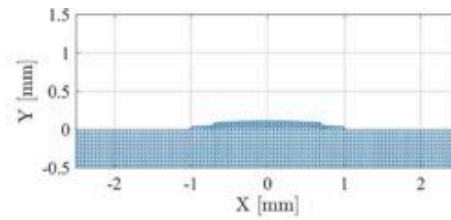
4.1. Computational results

The implementation of the FEM, Newton-Raphson
and material deposition model was executed in
595 MATLAB. Figure 8(a-f) show the evolution of the
bead geometry in the time interval that the laser spot
requires to engage, to heat and to leave behind the
relevant cross section. In this simulation, the deposi-
tion takes place from the time in which the substrate
600 reaches the material melting point (circa $t = 12\Delta t$).

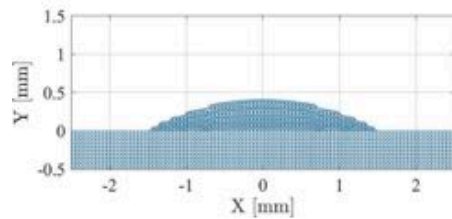
Figure 8(f) depicts the final shape of the domain.
The FEA mesh of the final domain has 21862 trian-
gular elements. Almost all the triangles in the FEA



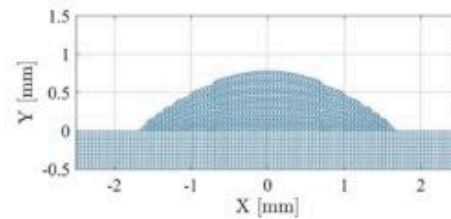
(a) Bead shape at $t = 0$. Triangles with aspect ratio
 < 3 : 100%.



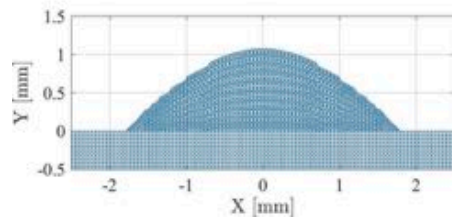
(b) Bead shape at $t = 13\Delta t$. Triangles with aspect ratio
 < 3 : 100%.



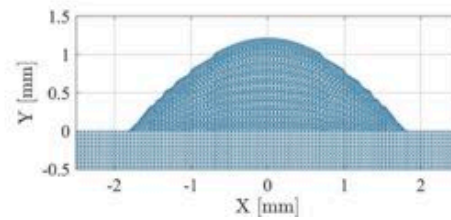
(c) Bead shape at $t = 16\Delta t$. Triangles with aspect ratio
 < 3 : 100%.



(d) Bead shape at $t = 19\Delta t$. Triangles with aspect ratio
 < 3 : 100%.



(e) Bead shape at $t = 22\Delta t$. Triangles with aspect ratio
 < 3 : 100%.



(f) Bead shape at $t = 25\Delta t$. Triangles with aspect ratio
 < 3 : 99.97%.

Figure 8. Evolution of the shape of the bead during deposition. Finer mesh resolution in the deposition region.

605 mesh had aspect ratio lower than 3 at all times in the simulation. In particular, in the final mesh 98.20% and 99.97% of the triangles have aspect ratio lower than 2 and 3, respectively.

610 Figure 8(f) shows that the final bead height and width are 1.22 mm and 3.68 mm, respectively. For a physical experiment with the same materials and conditions of this simulation, Ref. (Cordovilla et al. 2019) reported a bead height of 1.067 mm and a bead width of 4.697 mm. Figure 9 shows a graphical scheme of the geometrical involved in the comparison between the numerical and experimental results in (Cordovilla et al. 2019). The relative errors between

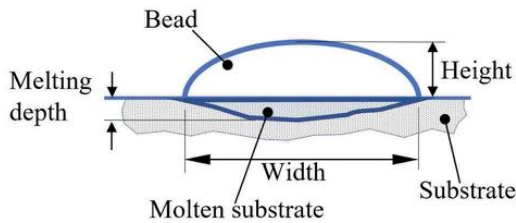


Figure 9. Sketch on the semantics of the geometrical parameters in Ref. (Cordovilla et al. 2019). (Contains typical names used in the related literature).

the simulated and the experimental (Cordovilla et al. 2019) bead height and width are 14.4% and 21.7%, respectively.

620 Figure 10(a–i) depict the substrate and bead temperature fields. While the laser energy is being delivered at this particular cross section, the highest temperature appears at the top of the bead. This trend is expected, as this neighbourhood directly receives the molten metal and the laser energy. Figure 10(f–i) correspond to the metal dispenser nozzle no longer delivering energy or material at this particular cross section. Between $t = 25\Delta t$ (Figure 10(f)) and $t = 34\Delta t$ (Figure 10(i)), the temperature of the bead decreases whereas the temperature in the substrate does not suffer large variations.

635 Figure 11 displays the temperature history at four locations: (1) the top point of the bead, (2) the top of the substrate, (3) 0.3 mm depth in the substrate and (4) 0.6 mm depth in the substrate. The top of the bead and the top of the substrate coincide until the start of the deposition. The temperature of the substrate increases rapidly while it interacts directly with the laser. It stabilises during the deposition stage and decreases once the bead cools down. The results of the simulation show that 0.6 mm is the largest depth at

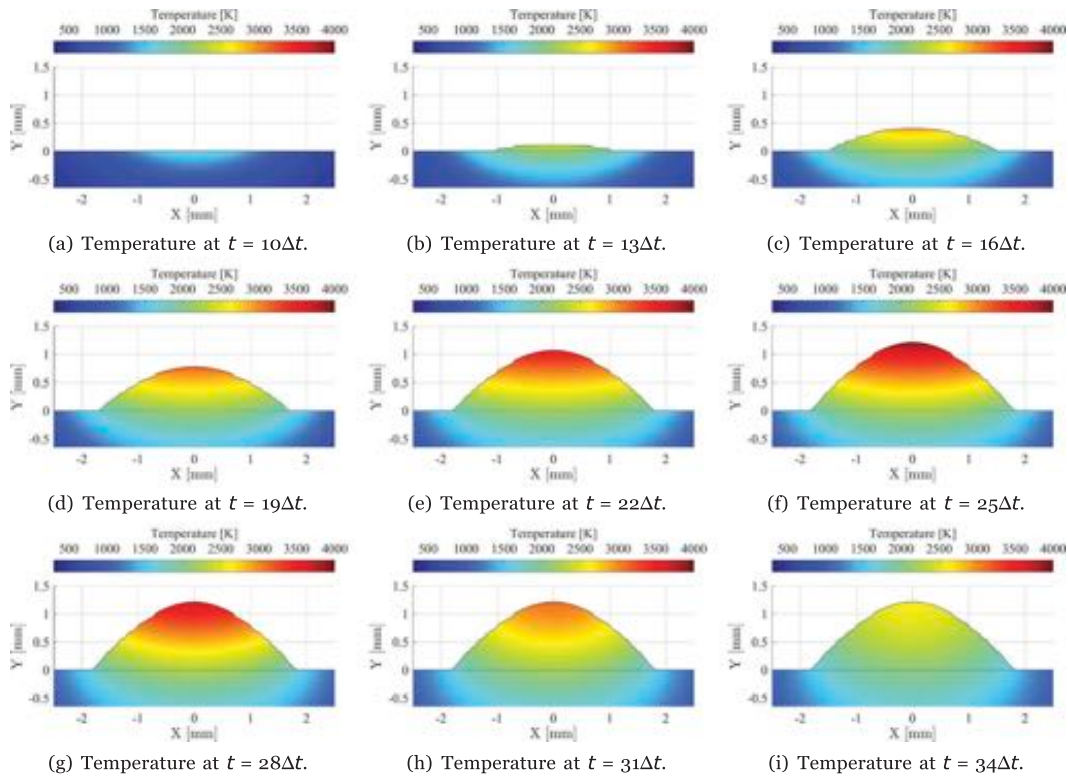


Figure 10. Temperature field of the cladding zone during deposition.

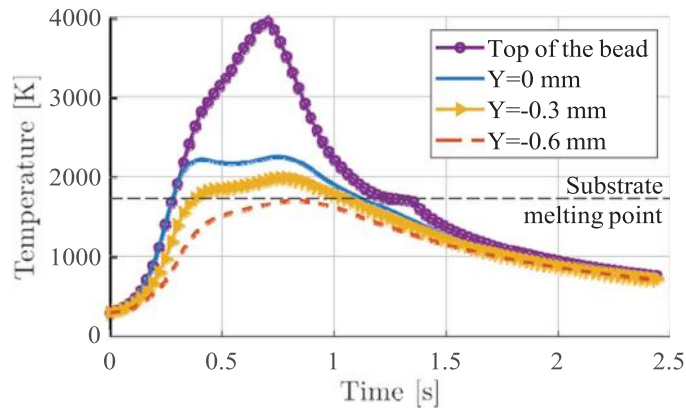


Figure 11. Temperature history at the top of the bead and substrate depths 0 mm, 0.3 mm and 0.6 mm.

which the substrate melts. Experimentally, Ref. (Ravi et al. 2013) reports a melting depth of 0.36 mm. This discrepancy is discussed in Section 4.2.

The temperature of the top of the bead increases in the presence of the laser and quickly decreases in the absence of it. The heat in the bead dissipates due to (1) conduction to the substrate, and (2) radiation and convection. The temperature plateau registered at the top of the bead around $T_m = 1690.5$ K corresponds to a phase change. An amount of energy is released by the system due to the solidification of the powder while temperature remains constant. The maximum simulation temperature is close to 4000 K. Other numerical simulations report similar temperature values for stainless steel under comparable ratios of power per powder deposition rate (Ya, Pathiraj, and Liu 2016).

4.2. Discussion

This section discusses the discrepancies between the numerical predictions of the non-linear 2.5D implementation reported here and experimental work by other investigators. The comparison is carried out with respect to Ref. (Cordovilla et al. 2019). It represents, with this manuscript, two prongs of a common initiative.

An important remark about experimental measurements in LMD is that direct temperature measurement is not feasible within the bead and substrate and very difficult on the bead surface at the melting time. Experimental investigations resort to the after-process cross-sectioning of the bead and substrate and indirect inference of the temperatures reached by observation of the metal micro-structures (Chua, Ahn, and Moon 2017; Tang et al. 2020).

There are several experimental effects that are not accounted for in the in-house non-linear FEA implementation:

1. An important portion (near 50%) of the powder metal delivered by the nozzle and heated by the laser does not reach the bead and deforms the space

distribution of the powder and power input (Ya, Pathiraj, and Liu 2016; Pinkerton 2015). The present implementation does not consider this effect, therefore over-estimating the power input in the energy balance. A consequence of this neglect is the over-estimation of molten depth (67% error) and bead temperature.

2. A significant portion of the laser power is lost to the environment by direct radiation, convection, and reflection by the powder.

3. Metal powder vaporisation produces mass and energy losses. Proposals have been published (Bayat et al. 2021; Gu and Li 2019; Song et al. 2020) to account for such losses in LMD and AM (e.g. powder bed fusion). Required parameters include vaporisation rate, boiling point and latent heat of vaporisation.

4. Molten powder fluid dynamics transforms part of the thermal energy in fluid friction. Parameters required include molten metal viscosity and surface tension.

The present implementation uses two 2D radial Gaussian distributions, mathematically defined in a plane (x, z) parallel to the substrate surface: (i) laser power and (ii) metal powder distribution. The experiments show that the Gaussian distributions incorrectly emphasise power and powder deliver at the laser axis, thus predicting a sharper deposition (i.e. smaller spot). In reality, the bead height is lower and the bead extent is wider than in the prediction. This result is also influenced by effect (1) above.

The absorption coefficient (λ) in the literature (Arrizubieta et al. 2017; Tian et al. 2019; Stender et al. 2018) expresses the portion of the laser power actually delivered to the bead-substrate domain. This parameters must be calibrated via experimentation. Likewise, all of the effects mentioned above imply the use of new experimentally calibrated parameters. This manuscript does not intend to contribute in this realm.

Table 4 summarises the numerical and experimental results for the bead height, bead width and melting depth. The relative error in Table 4 measures the deviation of the numerical result with respect to the

Table 4. Comparison between the numerical simulation and the experimental results reported in [Ref.-\(Cordovilla et al. 2019\)](#).

Parameter	Numerical result	Experimental result	Relative error
Bead height	1.22 mm	3.68 mm	14.4%
Bead width	1.067 mm	4.697 mm	21.7%
Melting depth	0.6 mm	0.36 mm	66.7%

experimental result. The error in the estimation of the melting depth is related to an over-estimation of the temperature field during simulation. The causes for the temperature over-estimation and bead width under-estimation are the ones discussed above.

5. Conclusions

This manuscript presents the implementation of a nonlinear thermal simulation to model the Laser Metal Deposition (LMD) process. The implementation considers temperature-dependent material properties, phase change, radiation and convection. The energy of the laser is represented as an energy flux boundary condition. The manuscript details the mathematical derivation of the FEM implementation. The nonlinear iterations inherent to each particular time step are executed using the Newton-Raphson method. The nonlinear FEM implementation is written for triangular 2D-plus-thickness elements. The LMD model is dictated by the delivery rate of powder (feed rate μ [kg/s]) and its associated Gaussian function of the radii from the nozzle axis. The model does not assume a particular geometry (parabolic, circular, sinusoidal, etc.) for the bead cross-section, as some previous works do.

Computer simulations are conducted using material and process parameters whose experimental counterpart is already reported in [Ref.\(Ravi et al. 2013\)](#). The results show reasonable accuracy to predict bead geometry (width error 15%, height error 22%). The model over-estimates the temperature at the domain and the maximal depth, in the substrate, at which melting occurs. The absorption coefficient (λ), which expresses the portion of the laser power input to the bead-substrate domain requires further investigation. It is affected by phenomena not yet understood or even identified. It is not the intention or capacity of this manuscript to contribute in this realm. Future work is also needed to account for the particle (thermo) dynamics over the substrate, responsible for a significant material and energy waste.

Glossary

AM
Additive manufacturing.

FEA
Finite element analysis.

FEM
Finite element method.

LMD
Laser metal deposition.

PL
Piecewise linear.

$\Omega \subset \mathbb{R}^2$
2D-plus-thickness FEA domain.

$\partial\Omega$
1D border of domain Ω .

$M = (V, T)$
FEA triangular mesh defined by the set of nodes V and the set of triangles T .

$\Delta z \in \mathbb{R}$
Thickness of the domain Ω [mm]

$\Delta t \in \mathbb{R}$
Time increment for the FEM simulation [s]

$T(\mathbf{x}, t) : \mathbb{R}^2 \times \mathbb{R} \rightarrow \mathbb{R}$
Temperature at $\mathbf{x} \in \Omega$ in the instant t [K]

$T^h(\mathbf{x}, t) : \mathbb{R}^2 \times \mathbb{R} \rightarrow \mathbb{R}$
Approximated temperature function at $\mathbf{x} \in \Omega$ in the instant t [K]. It is the result given by the finite element method.

$\theta(t) : \mathbb{R} \rightarrow \mathbb{R}^{N_{nodes}}$
Global vector of nodal temperatures at time t [K].

$\theta^s \in \mathbb{R}^{N_{nodes}}$
Global vector of nodal temperatures at time t^s [K].

$\theta^{s,k} \in \mathbb{R}^{N_{nodes}}$
Global vector of nodal temperatures at time t^s and iteration k in the Newton-Raphson scheme [K].

$M(\mathbf{x}, t) : \mathbb{R}^2 \times \mathbb{R} \rightarrow \mathbb{R}^{N_{nodes}} \times \mathbb{R}^{N_{nodes}}$
Global mass matrix in the FEM formulation [J/K].

$M^s(\mathbf{x}, t) : \mathbb{R}^2 \times \mathbb{R} \rightarrow \mathbb{R}^{N_{nodes}} \times \mathbb{R}^{N_{nodes}}$
Global mass matrix at time t^s [J/K].

$\mathbb{K}(\mathbf{x}, t) : \mathbb{R}^2 \times \mathbb{R} \rightarrow \mathbb{R}^{N_{nodes}} \times \mathbb{R}^{N_{nodes}}$
Global conductivity matrix in the FEM formulation [W/K].

$\mathbb{K}^s(\mathbf{x}, t) : \mathbb{R}^2 \times \mathbb{R} \rightarrow \mathbb{R}^{N_{nodes}} \times \mathbb{R}^{N_{nodes}}$
Global conductivity matrix at time t^s [J/K].

$\mathbf{f}(\mathbf{x}, t) : \mathbb{R}^2 \times \mathbb{R} \rightarrow \mathbb{R}^{N_{nodes}}$
Global force vector in the FEM formulation [W].

$\mathbf{f}^s(\mathbf{x}, t) : \mathbb{R}^2 \times \mathbb{R} \rightarrow \mathbb{R}^{N_{nodes}}$
Global force vector at time t^s [W].

765

770

775

780

785

790

795

800

805

810

815

820

825

830	$T^0(\mathbf{x}) : \mathbb{R}^2 \rightarrow \mathbb{R}$ Initial (at $t = 0$) temperature at \mathbf{x} [K]	$f(x, z, t) : \mathbb{R}^2 \times \mathbb{R} \rightarrow \mathbb{R}$ Powder particle distribution projected by the nozzle onto the substrate at time t [$\text{kg}/(\text{mm}^2 \text{ s})$].	895
835	$\bar{T}(\mathbf{x}, t) : \mathbb{R}^2 \times \mathbb{R} \rightarrow \mathbb{R}$ Temperature function at the region with Dirichlet boundary conditions [K]	$H(x, z, t) : \mathbb{R}^2 \times \mathbb{R} \rightarrow \mathbb{R}$ Height of the bead at time t [mm].	900
840	$\bar{q}(\mathbf{x}, t) : \mathbb{R}^2 \times \mathbb{R} \rightarrow \mathbb{R}$ Heat flux function at the region with Neumann boundary conditions [W/m^2]	$L \in \mathbb{R}$ Latent heat of fusion [J/kg].	
840	R System of nonlinear equations associated to the semi-discrete FEM formulation.	$h_c \in \mathbb{R}$ Convection coefficient [$\text{W}/(\text{m}^2 \text{ K})$].	905
845	$\mathbf{q}(\mathbf{x}, t) : \mathbb{R}^2 \times \mathbb{R} \rightarrow \mathbb{R}^2$ Heat flux into or out of the medium at $\mathbf{x} \in \Omega$ at time t [W/m^2]	$\varepsilon \in \mathbb{R}$ Material thermal emissivity.	910
850	$s(\mathbf{x}, t) : \mathbb{R}^2 \times \mathbb{R} \rightarrow \mathbb{R}$ Volumetric heat sources at $\mathbf{x} \in \Omega$ in the instant t [W/m^3]	$\sigma \in \mathbb{R}$ Stefan-Boltzmann constant [$\text{W}/(\text{m}^2 \text{ K}^4)$].	
850	$\mathbf{n}(\mathbf{x}) : \mathbb{R}^2 \rightarrow \mathbb{R}^2$ Outward unit normal to the boundary at $\mathbf{x} \in \Omega$	$T_\infty \in \mathbb{R}$ Ambient temperature [K].	915
855	$\rho(T) : \mathbb{R} \rightarrow \mathbb{R}$ Density of the material [kg/m^3] as a function of the temperature.	Data Availability Statement	Q7
860	$\kappa(T) : \mathbb{R} \rightarrow \mathbb{R}$ Thermal conductivity of the material [$\text{W}/(\text{m K})$] as a function of the temperature.	The authors confirm that the data supporting the findings of this study are available within the article.	
865	$C(T) : \mathbb{R} \rightarrow \mathbb{R}$ Specific heat capacity of the material [$\text{J}/(\text{kg K})$] as function of the temperature.	Disclosure statement	920
870	$N_1(\xi, \eta), N_2(\xi, \eta), N_3(\xi, \eta) : \mathbb{R}^2 \rightarrow \mathbb{R}$ Shape functions in the FEM formulation for 3-node triangular elements. Interpolation functions inside the triangular elements.	No potential conflict of interest was reported by the author(s).	Q8
875	$N_1^q(\xi), N_2^q(\xi) : \mathbb{R} \rightarrow \mathbb{R}$ Shape functions in the FEM formulation for the edges of 3-node triangular elements. Interpolation functions along the edges with Neumann boundary conditions.	Funding	
880	$I(x, z, t) : \mathbb{R}^2 \times \mathbb{R} \rightarrow \mathbb{R}$ Laser energy intensity distribution [W/mm^2]	This work has received funding from the Eusko Jaurlaritza/Basque Government under the grants KK-2018/00115 (ADDISEND) and KK-2018/00071 (LANGILEOK).	925
885	$P_L \in \mathbb{R}$ Laser nominal power [W]		Q9
890	$R_L \in \mathbb{R}$ Laser beam radius [W]	ORCID	
	$[T_s, T_l] \subset \mathbb{R}$ Melting range of the material [K].	Diego Montoya-Zapata  http://orcid.org/0000-0001-5521-1794	
	$\mu \in \mathbb{R}$ Material flow rate [kg/s]	Aitor Moreno  http://orcid.org/0000-0002-9088-7332	930
		Oscar Ruiz-Salguero  http://orcid.org/0000-0002-9674-8974	
		Jorge Posada  http://orcid.org/0000-0001-7985-9915	
		References	935 Q10
		Arrizubieta, J. I., A. Lamikiz, F. Klocke, S. Martínez, K. Arntz, and E. Ukar. 2017. "Evaluation of the Relevance of Melt Pool Dynamics in Laser Material Deposition Process Modeling." <i>International Journal of Heat and Mass Transfer</i> 115: 80–91. doi:10.1016/j.ijheatmasstransfer.2017.07.011.	940
		Bakhshi, S. 2018. "Numerical Analysis to Study the Effect of Sag and Non-circular Whirl Orbits on the Damping Performance of a Squeeze Film Damper." Master's thesis, Cincinnati, USA: University of Cincinnati.	945
		Bayat, M., V. K. Nadimpalli, F. G. Biondani, S. Jafarzadeh, J. Thorborg, N. S. Tiedje, G. Bissacco, D. B. Pedersen, and J. H. Hattel. 2021. "On the Role of the Powder Stream on	

- the Heat and Fluid Flow Conditions during Directed Energy Deposition of Maraging steel—Multiphysics Modeling and Experimental Validation.” *Additive Manufacturing* 43: 102021. doi:10.1016/j.addma.2021.102021.
- Bergheau, J.-M., and R. Fortunier. 2008. “Non-linearities.” *Finite Element Simulation of Heat Transfer*, 143–167. ch. 5. John Wiley & Sons.
- Caiazza, F., and V. Alfieri. 2019. “Simulation of Laser-assisted Directed Energy Deposition of Aluminum Powder: Prediction of Geometry and Temperature Evolution.” *Materials* 12 (13): 2100. doi:10.3390/ma12132100.
- Carbonell, J. M., J. M. Rodríguez, and E. Oñate. 2020. “Modelling 3D Metal Cutting Problems with the Particle Finite Element Method.” *Computational Mechanics* 66 (3): 603–624. doi:10.1007/s00466-020-01867-5.
- Cheng, B., S. Shrestha, and K. Chou. 2016. “Stress and Deformation Evaluations of Scanning Strategy Effect in Selective Laser Melting.” *Additive Manufacturing* 12: 240–251. doi:10.1016/j.addma.2016.05.007.
- Chua, Z. Y., I. H. Ahn, and S. K. Moon. 2017. “Process Monitoring and Inspection Systems in Metal Additive Manufacturing: Status and Applications.” *International Journal of Precision Engineering and Manufacturing-Green Technology* 4 (2): 235–245. doi:10.1007/s40684-017-0029-7.
- Corbin, D. J., A. R. Nassar, E. W. Reutzler, A. M. Beese, and N. A. Kistler. May 2017. “Effect of Directed Energy Deposition Processing Parameters on Laser Deposited Inconel 718: External Morphology.” *Journal of Laser Applications* 29: 022001. doi:10.2351/1.4977476.
- Cordova, F., P. Álvarez, A. García-Beltrán, M. A. Montealegre, and J. Ocaña. 2019. *Non-linear Thermal Model of the Direct Laser Melting Process considering the Adhesion of the Consolidated Material to the Substrate Using a Domain with Discontinuous Material Properties*. Proceedings of Lasers in Manufacturing.
- Costa, L., T. Reti, A. Deus, and R. Vilar. 2002. “Simulation of Layer Overlap Tempering Kinetics in Steel Parts Deposited by Laser Cladding.” In *Proceedings of International Conference on Metal Powder Deposition for Rapid Manufacturing*, 172–176. Princeton, NJ: MPIF.
- El Cheikh, H., B. Courant, S. Branchu, J.-Y. Hascoët, and R. Guillén. 2012. “Analysis and Prediction of Single Laser Tracks Geometrical Characteristics in Coaxial Laser Cladding Process.” *Optics and Lasers in Engineering* 50 (3): 413–422. doi:10.1016/j.optlaseng.2011.10.014.
- Engwirda, D. 2014. “Locally optimal Delaunay-refinement and optimisation-based mesh generation.” PhD thesis, University of Sydney.
- Farahmand, P., and R. Kovacevic. 2014. “An Experimental-numerical Investigation of Heat Distribution and Stress Field in Single- and Multi-track Laser Cladding by a High-power Direct Diode Laser.” *Optics & Laser Technology* 63: 154–168. doi:10.1016/j.optlastec.2014.04.016.
- Goodarzi, D. M., J. Pekkarinen, and A. Salminen. February 2015. “Effect of Process Parameters in Laser Cladding on Substrate Melted Areas and the Substrate Melted Shape.” *Journal of Laser Applications* 27: S29201. doi:10.2351/1.4906376.
- Gu, H., and L. Li. 2019. “Computational Fluid Dynamic Simulation of Gravity and Pressure Effects in Laser Metal Deposition for Potential Additive Manufacturing in Space.” *International Journal of Heat and Mass Transfer* 140: 51–65. doi:10.1016/j.ijheatmasstransfer.2019.05.081.
- Heigel, J., P. Michaleris, and T. Palmer. 2015. “In Situ Monitoring and Characterization of Distortion during Laser Cladding of Inconel 625.” *Journal of Materials Processing Technology* 220: 135–145. doi:10.1016/j.jmatprotec.2014.12.029.
- Ibrahimbegovic, A. 2009. *Nonlinear Solid Mechanics: Theoretical Formulations and Finite Element Solution Methods*. Vol. 160. Springer Science & Business Media.
- Leino, M., J. Pekkarinen, and R. Soukka. 2016. “The Role of Laser Additive Manufacturing Methods of Metals in Repair, Refurbishment and Remanufacturing – Enabling Circular Economy.” *Physics Procedia* 83: 752–760. doi:10.1016/j.phpro.2016.08.077.
- Manvatkar, V., A. De, and T. DebRoy. 2015. “Spatial Variation of Melt Pool Geometry, Peak Temperature and Solidification Parameters during Laser Assisted Additive Manufacturing Process.” *Materials Science and Technology* 31 (8): 924–930. doi:10.1179/1743284714Y.0000000701.
- Mayi, Y. A., M. Dal, P. Peyre, M. Bellet, C. Metton, C. Moriconi, and R. Fabbro. 2020. “Laser-induced Plume Investigated by Finite Element Modelling and Scaling of Particle Entrainment in Laser Powder Bed Fusion.” *Journal of Physics D: Applied Physics* 53 (7): 075306. doi:10.1088/1361-6463/ab5900.
- Michaleris, P. 2014. “Modeling Metal Deposition in Heat Transfer Analyses of Additive Manufacturing Processes.” *Finite Elements in Analysis and Design* 86: 51–60. doi:10.1016/j.finel.2014.04.003.
- Mills, K. C. 2002. “Fe Pure Iron.” In *Recommended Values of Thermophysical Properties for Selected Commercial Alloys*, edited by K. C. Mills, 105–112. Woodhead Publishing Series in Metals and Surface Engineering. Woodhead Publishing.
- Montoya-Zapata, D., C. Creus, A. Moreno, I. Ortiz, P. Alvarez, O. Ruiz-Salguero, and J. Posada. 2021a. “Computational Minimization of Over-deposition at Corners of Trajectories in Laser Metal Deposition.” *Manufacturing Letters* 29: 29–33. doi:10.1016/j.mfglet.2021.05.001.
- Montoya-Zapata, Diego, Juan M. Rodríguez, Aitor Moreno, Jorge Posada, Oscar Ruiz-Salguero, N. Lebaal, S. Jayanthi, J. Davidson, and M.C. Lemmbabu. 2021b. “2D Linear Finite Element Simulation of Laser Metal Heating for Digital Twins.” *International Journal of Simulation and Multidisciplinary Design Optimization* 12: 11. doi:10.1051/smdo/2021011.
- Nenadl, O., V. Ocelik, A. Palavra, and J. T. De Hosson. 2014. “The Prediction of Coating Geometry from Main Processing Parameters in Laser Cladding.” *Physics Procedia* 56: 220–227. 8th International Conference on Laser Assisted Net Shape Engineering LANE.
- Ocelik, V., O. Nenadl, A. Palavra, and J. De Hosson. 2014. “On the Geometry of Coating Layers Formed by Overlap.” *Surface and Coatings Technology* 242: 54–61. doi:10.1016/j.surfcoat.2014.01.018.
- Pinkerton, A. J. 2015. “Advances in the Modeling of Laser Direct Metal Deposition.” *Journal of Laser Applications* 27 (S1): S15001. doi:10.2351/1.4815992.
- Ravi, G., X. Hao, N. Wain, X. Wu, and M. Attallah. 2013. “Direct Laser Fabrication of Three Dimensional Components Using SC420 Stainless Steel.” *Materials & Design* 47: 731–736. doi:10.1016/j.matdes.2012.12.062.

Q11

985

990

995

1000

1005

1010

Q12

Q13

1015

1020

1025

1030

1035

1040

1045

1050

1055

1060

1065

1070

1075

1080

- Rodriguez, J. M., J. M. Carbonell, J. C. Cante, and J. Oliver. 2016. "The Particle Finite Element Method (PFEM) in Thermo-mechanical Problems." *International Journal for Numerical Methods in Engineering* 107 (9): 733–785. doi:10.1002/nme.5186. 1085
- Shewchuk, J. R. 1996. "Triangle: Engineering a 2D Quality Mesh Generator and Delaunay Triangulator." In *Applied Computational Geometry Towards Geometric Engineering*, edited by M. C. Lin and D. Manocha, 203–222. Berlin, Heidelberg: Springer Berlin Heidelberg. 1090
- Song, B., T. Yu, X. Jiang, W. Xi, and X. Lin. 2020. "Effect of Laser Power on Molten Pool Evolution and Convection." *Numerical Heat Transfer, Part A: Applications* 78 (2): 48–59. doi:10.1080/10407782.2020.1777795.
- Sorkine, O., D. Cohen-Or, Y. Lipman, M. Alexa, C. Rössl, and H.-P. Seidel. 2004. "Laplacian Surface Editing." In *Proceedings of the 2004 Eurographics/ACM SIGGRAPH Symposium on Geometry Processing, SGP '04*, pp. 175–184. New York, NY, USA: Association for Computing Machinery. 1100
- Stender, M. E., L. L. Beghini, J. D. Sugar, M. G. Veilleux, S. R. Subia, T. R. Smith, C. W. S. Marchi, A. A. Brown, and D. J. Dagle. 2018. "A Thermal-mechanical Finite Element Workflow for Directed Energy Deposition Additive Manufacturing Process Modeling." *Additive Manufacturing* 21: 556–566. doi:10.1016/j.addma.2018.04.012. 1105
- Taberero, I., A. Lamikiz, E. Ukar, L. López de Lacalle, C. Angulo, and G. Urbikain. 2010. "Numerical Simulation and Experimental Validation of Powder Flux Distribution in Coaxial Laser Cladding." *Journal of Materials Processing Technology* 210 (15): 2125–2134. doi:10.1016/j.jmatprotec.2010.07.036. 1110
- Taberero, I., A. Lamikiz, E. Ukar, S. Martnez, and A. Celaya. 2013. "Modeling of the Geometry Built-up by Coaxial Laser Material Deposition Process." *The International Journal of Advanced Manufacturing Technology* 70 (5): 843–851. doi:10.1007/s00170-013-5284-3. 1115
- Tamanna, N., R. Crouch, and S. Naher. 2019. "Progress in Numerical Simulation of the Laser Cladding Process." *Optics and Lasers in Engineering* 122: 151–163. doi:10.1016/j.optlaseng.2019.05.026. 1120
- Tang, Z., W. Liu, Y. Wang, K. M. Saleheen, Z. Liu, S. Peng, Z. Zhang, and H. Zhang. 2020. "A Review on in Situ Monitoring Technology for Directed Energy Deposition of Metals." *The International Journal of Advanced Manufacturing Technology* 108 (11–12): 3437–3463. doi:10.1007/s00170-020-05569-3. 1125
- Tian, H., X. Chen, Z. Yan, X. Zhi, Q. Yang, and Z. Yuan. 2019. "Finite-element Simulation of Melt Pool Geometry and Dilution Ratio during Laser Cladding." *Applied Physics A* 125 (7). doi:10.1007/s00339-019-2772-9. 1130
- Ya, W., B. Pathiraj, and S. Liu. 2016. "2D Modelling of Clad Geometry and Resulting Thermal Cycles during Laser Cladding." *Journal of Materials Processing Technology* 230: 217–232. doi:10.1016/j.jmatprotec.2015.11.012. 1135
- Zhou, S., X. Dai, and H. Zheng. 2011. "Analytical Modeling and Experimental Investigation of Laser Induction Hybrid Rapid Cladding for Ni-based WC Composite Coatings." *Optics & Laser Technology* 43 (3): 613–621. doi:10.1016/j.optlastec.2010.09.001. 1140
- Zhu, J., M. Khurshid, and Z. Barsoum. 2019. "Accuracy of Computational Welding Mechanics Methods for Estimation of Angular Distortion and Residual Stresses." *Welding in the World* 63 (5): 1391–1405. doi:10.1007/s40194-019-00746-9. 1145